JPC 430

Report Number
F-66-10

Investigation of High Acceleration on the Interior Ballistics of Solid Propellant Rocket Motors

by

B. W. Farquhar

D. J. Norton

J. D. Hoffman

Final Report

AMC Contract Number DA-01-021-AMC-12864(Z)

December 1966

JET PROPULSION CENTER
PURDUE UNIVERSITY

SCHOOL OF MECHANICAL ENGINEERING
LAFAYETTE, INDIANA

ACKNOWLEDGMENTS

The research investigation described in this final report was supported by the United States Army Missile Command, Redstone Arsenal, Alabama, under Contract Number DA-021-AMC-12864(z). This study was initiated by the same agency under a previous contract, DA-01-021-AMC 428(z) D4-13612. Mr. W. D. Guthrie was technical monitor for the U. S. Army Missile Command.

Professor Emeritus Dr. M. J. Zucrow and Dr. B. A. Reese, Director of the Jet Propulsion Center, Purdue University, are gratefully acknowledged for contributing their knowledge and experience. The labors of Dr. Mel L'Ecuyer, of the Jet Propulsion Center, Purdue University, who has recently acquired the responsibility of supervising this research, are appreciated. The contributions of Mr. G. R. Johnson, a Master's degree candidate at Purdue University, also deserve recognition.

PURDUE UNIVERSITY

AND

PURDUE RESEARCH FOUNDATION
Lafayette, Indiana

Report No. F-66-10

INVESTIGATION OF HIGH ACCELERATION ON THE INTERIOR BALLISTICS OF SOLID PROPELLANT ROCKET MOTORS

by

B. W. Farquhar, D. J. Norton, J. D. Hoffman

Final Report

Contract No. DA-01-021-AMC-12864(Z)

United States Army Missile Command

Redstone Arsenal, Alabama

Jet Propulsion Center
Purdue University

December 1966

TABLE OF CONTENTS

LIST OF ILLUSTRATIONS

ABSTRACT

This report is the final report describing the work accomplished from July, 1964 to September, 1966 on the investigation of the effects of high acceleration on the interior ballistics of solid propellant rocket motors. A description of the cold flow spin test apparatus and instrumentation is presented. The results of some of the preliminary tests are given and the program for future testing is described. An analytical study is presented which describes various simplified models which account for the effects of rotation on the mass flow and thrust producing capabilities of the nozzle. Results are given for two limiting cases:

1. Uniform axial velocity profiles at each plane in the nozzle.
2. Uniform angular velocity profiles at each plane in the nozzle.

These cases are discussed and a more advanced model is formulated. The complete model is described and future analytical computations are discussed.

BLANK PAGE

I. INTRODUCTION

In the early stages of development of spin stabilized missiles it was observed that the ballistic performance of spinning missiles differed quite drastically from the performance of non-spinning missiles. The spinning solid propellant rocket motor was usually characterized by a shorter propellant burning time, an erratic pressure-time trace with rather high pressure peaks, and thrust-time curves differing appreciably from the performance of non-spinning motors. A considerable amount of work, discussed in References 1 and 2, has been done in an attempt to determine how spin affects the ballistic performance of a solid propellant rocket motor.

The purpose of this research was to study the effect of spin on a solid propellant rocket motor and to develop a technique for predicting the performance of spinning solid propellant rocket motors. The analytical and experimental work completed to date on this project are described in this report.

II. EXPERIMENTAL INVESTIGATION

The primary objective of the experimental part of this program was to study the effects of rotation of a solid propellant rocket motor on the internal ballistics of the motor. Two approaches to this study were considered: (1) actual firing of various solid propellants using several grain designs, nozzle contraction ratios and spin rates, and (2) a cold flow study utilizing air in a rocket motor which permitted simulation of various grain designs, variable flow rates, multiple contraction ratios, and a range of spin rates. The cold flow study also offered the possibility of the use of flow probes for determining flow characteristics inside the rocket motor. The high temperatures occurring in actual firings precluded the use of probes in such cases. Also, a considerable number of studies have been conducted previously on actual firings of spinning rockets. Therefore, a cold flow study appeared to be the most fruitful.

The design of the cold flow spinning rocket motor, henceforth referred to as a spin rig, was based on the following criteria:

1. Rotational velocities from 0 to 25,000 rpm must be attainable.
2. The system must be able to measure thrust loads of 600 lbf.
3. The spinning simulated rocket motor should reproduce as closely as possible the actual flow conditions existing in a spinning rocket motor.
4. The system should allow the probing of the flow field to obtain pressure and velocity distributions.

5. The spin rig must be able to accomodate various size rocket motors, both actual and cold flow, having internal diameters up to 7 inches and lengths up to 18 inches.

6. The nozzle design must incorporate various contraction ratios.

7. A variable mass flow between 1 lbm/sec and 10 lbm/sec must be possible.

Using these guide lines, an apparatus was constructed which consists of the following three basic systems:

1. The rocket motor, simulated grains and bearing system.
2. The air feed system which supplies air to the motor.
3. The driver which rotates the motor.

Figure 1 is a photograph of the spin rig. The rocket motor is supported horizontally on four bearings, two of which are mounted at the nozzle. The remaining two are located on the driving shaft on each side of the air chamber. All the bearings used so far are class 7, mist lubricated ball bearings. The motor casing is 18 inches long, 6 inches internal diameter, and is made of 440 C stainless steel to accommodate the high stresses due to the angular acceleration loading. Two nozzles were fabricated with throat diameters of 1.2 inches and 2.0 inches. The combined length of the motor casing and the nozzle is approximately 24 inches.

Figure 2 shows the system of inserts used to simulate an end-burning grain. This simulated grain consists of a 1 inch thick aluminum plate containing approximately 600 holes of 1/8 inch diameter drilled symmetrically about the axis of rotation. This plate is held in position by a system of aluminum sleeves of various lengths allowing the location of the plate to be varied along the axis of the motor.

Figure 3 shows the simulated internal-burning cylindrical grain. This grain is an aluminum tube 13 inches long containing approximately 400, 1/4 inch diameter holes drilled radially and staggered on circumferential circles along the length of the tube. This tube is supported in place inside the motor with end plates. The upstream plate is ported to allow the air to flow between the chamber wall and the grain. Both grains are held in place inside the chamber by the nozzle.

Figure 4 is a schematic drawing of the cold flow air system. Air is supplied to the motor from a large set of receivers initially at a pressure of 2,500 psig. The pressure is reduced to approximately 1000 psig through a regulator. It then flows through a separator, a filter, an orifice and flow control valve, and then on to the air feed chamber.

The air feed chamber, shown in Fig. 5, is located at the fore-end of the spin rig. The air flowing to the air feed chamber passes through slots in the drive shaft into a one inch diameter hole in the drive shaft and then into the spinning motor. Balanced mechanical seals located in the bearing housing restrict the air leakage around the drive shaft. The entire rotating assembly is rigidly supported by two, 2.5 inch diameter rods which in turn are mounted in linear bearings allowing horizontal movement for thrust measurements. Thrust is measured by two load cells located at the end of these rods. Two springs attached to the front bearing support keep the load cells preloaded. Each rotating component of the spin rig has been dynamically balanced and the entire assembled unit has been dynamically balanced.

The first system used to drive the spin motor was a 7.5 hp, varispeed, 5000 rpm electric motor. This motor was connected to an oil lubricated speed increasing gear (approximate ratio 3:1) using a system of sheaves and cog belts. The input speed to the gear increaser could be increased by changing the sheave on the vari-speed motor. The speed increasing gear was direct-connected to the shaft of the spinning motor with a Falk, high speed, gear type coupling. Initial running tests with this drive arrangement allowed speeds up to 5000 rpm with an air mass flow rate of about 5 lbm/sec. At higher speeds or with greater mass flows the vari-speed drive was overloaded. This limitation required that a new driver system be employed to replace the varispeed electric motor. This was accomplished by using a 25,000 rpm, 8 inch diameter wheel, Barbour-Stockwell air turbine which was direct connected to the spin rig drive shaft through a 5/8 inch quill shaft.

The instrumentation available on the spin rig consists of a strain gage pressure transducer to measure the pressure drop at the flow orifice. Pressure gages are used to indicate the supply pressure before the regulator and static pressure at the orifice. Thermocouples are used to monitor the flow orifice temperature and the temperature of each bearing. An electronic counter and magnetic pickup are used to indicate the rotational speed of the spin motor. Various arrangements of pressure transducers, thermocouples and manometers are used for measurements with the flow probes.

Figure 6 shows a second test motor which has been constructed to characterize the performance of the injectors. This motor duplicates closely the dimensions of the existing motor except for length. It was

constructed of Plexiglas tubing with a 6 inch internal diameter and 1/2 inch wall thickness. A system of Plexiglas grain inserts was constructed for this motor. Three probe ports were installed in the wall of the cylinder between the grain and the nozzle to allow pressure and velocity to be measured across the face of the simulated grain. The Plexiglas motor uses the same nozzles as the spin motor. This Plexiglas motor is not designed to be rotated.

A probe traversing system has been constructed which is capable of moving a probe vertically through a distance of about 3 inches. This device is driven by a gear motor operated remotely from the control room. This probe traversing system is designed so that the flow may be probed through the throat in the case of the rotating motor, or through the casing wall in the case of the Plexiglas motor. Both pressure and hot wire probes may be used.

To date, most of the experimental data taken was concerned with establishing the operating ranges of the various parameters such as mass flow rate, angular speed and chamber pressures. Mass flow rates of 9.1 lbm/sec with the 2 inch diameter nozzle and rotational velocities of 5000 rpm have been attained. Higher spin rates have not been attempted yet due to balancing problems. At this mass flow rate the chamber pressure was approximately 86 psig and the temperature was 53°F. The chamber pressure and temperature were measured upstream of the simulated end-burning grain using a probe inserted through the throat and supported by a bearing in the grain.

Additional tests were conducted to investigate the effect, if any, that the rotation of the rocket motor had on the mass flow and chamber pressure. These studies did not yield any detectable deviation from conditions in the non-rotating motor. It is expected that there will be a measurable decrease in the ratio of the mass flow rate to the center-line chamber pressure at higher rotational speeds, as predicted by Norton's analysis (page 10).

Studies were conducted to determine if rotation affected pressure profiles just upstream of the throat of the nozzle. Figure 7 shows the probe and traversing mechanism. The probe consisted of a straight 1/4 inch diameter tube with a short taper at its end. The tapered end was aligned axially and the total pressure was measured across a radius of the nozzle throat. Several traverses were made at various flow conditions and rotational speeds. Reference conditions were also obtained at the same flow conditions with no rotation. The results are plotted in Figure 8. The ordinate is the ratio of the measured pressure at each radial position divided by the center line pressure. This pressure ratio is plotted against a non-dimensional radius referenced to the throat radius. Each curve is for a constant rotational speed and mass flow rate. By comparing the rotating and non-rotating conditions it can be seen that rotation caused the pressure to increase near the wall. Figure 9 presents a similar set of data taken at a smaller mass flow rate. A comparison of the two curves for the same rotational speed (see Figure 10) indicates a greater increase in the pressure at the wall for the smaller mass flow rate.

The Plexiglas motor was used to study the flow field inside the rocket motor under non-rotating conditions. The initial studies indicated that very high gas velocities existed within 1/2 inch of the wall of the cylinder. In the region from the center line out to within 1/2 inch of the wall, little or no flow occurred. This condition was measured at the face of the simulated end-burning grain and at two other positions approximately three and six inches downstream from the grain. It was apparent that the injection system being used was not duplicating the mass flow distribution of a solid propellent end-burning grain. Thus, a series of tests utilizing one and two baffles upstream of the simulated end-burning grain were initiated in an attempt to obtain a more uniform velocity distribution across the face of the grain. During these tests, a failure of the Plexiglas motor was experienced (Figure 11). This failure required the disassembly of the spin rig and the turbine to change all of the bearings and seals and repair other minor damage. After testing was resumed, a set of two baffles was designed and tested which yielded a velocity profile across the face of the simulated end-burning grain in which the velocity differed by less than 25% from the average velocity at any point across the grain except at the center line. Figure 12 is a photograph showing the complete insert arrangement of the spinning rocket motor with the baffle design presently being used. At the center line of the simulated end-burning grain no flow occurs because of a probe support located at this point.

It was found during some of the initial spin testing that the sleeves and simulated end-burning grain were not rotating at the same velocity as the motor casing. Therefore, additional modification of the spin motor and

inserts was necessary. The sleeve nearest the head end of the motor was keyed to the motor with four hardened steel pins. Each succeeding sleeve or baffle was in turn keyed to the preceeding piece so that the entire insert assembly rotated as one piece at the same velocity as the motor casing.

A new nozzle is being fabricated which will allow a range of high contraction ratios to be tested. When completed, a series of tests will be conducted on the spin rig to determine the effect of contraction ratio, mass flow rate and spin velocity on nozzle choking. These tests will utilize the simulated end-burning grain located at various axial positions in the rocket motor and the simulated internal-burning cylindrical grain.

A probe and probe traversing system are being developed which will allow investigation of the flow field inside the spinning motor. The probe to be used will be of a 5 port design which is intended to yield approximate measurements of velocity magnitudes and direction. The probe will enter the motor through the nozzle throat and be supported in the motor by the simulated grain insert. Axial traverses will be made at a fixed radial position. A different probe will be required for each radial position investigated.

A probe is being constructed to investigate the existence of back flow in the motor near the motor axis. This probe consist of two total pressure tubes mounted back to back to sense and direction change in the axial velocity. This system will utilize the same axial traversing system described previously.

III. THEORETICAL INVESTIGATION

A. Introduction

When a solid propellant rocket motor is spun about its axis at very high angular velocities, it has been found that the performance of that motor does not match the predictions of the usual internal ballistics calculations. In fact, a number of experimenters have shown that:

1. The pressure in the chamber increases.
2. The burning time decreases.
3. Under some conditions the total impulse decreases.

These changes in the gross performance of the rocket motor have been attributed to one or both of the following causes.

1. Acceleration effects upon the burning characteristics of the propellant.
2. Fluid mechanical effects in the chamber and nozzle of the motor.

Under the general category of acceleration effects, a number of phenomena can contribute to the overall change in the ballistic properties of the propellant. These are:

1. Mechanical changes in the propellant due to
   a) stress and strain,
   b) density gradients, and
   c) slump or deformation.
2. Compression or expansion of the combustion zone of the propellant, thus increasing or decreasing the heat transfer rate to the surface.

3. Retention of the dense phases of the propellant products at the surface of the propellant, resulting in

   a) pitting of the propellant, thereby increasing the surface area, and

   b) puddling of solid phases, thereby increasing heat transfer to the propellant.

4. Centrifuging out of condensed phases against the nozzle walls thereby reducing the total impulse of the motor.

Under the category of fluid mechanical effects the following factors are important.

1. Reduction of the mass flow and thrust producing capabilities of the nozzle due to

   a) void regions in the flow, and

   b) a decrease in the mass flux at the throat section.

2. Pressure increases in the chamber resulting in an increase in burning rate.

3. Uneven burning of the propellant due to pressure gradients throughout the grain.

4. Erosive burning set up by vortex motion.

The basic difference between the flow in a rotating rocket motor and a nonrotating one is the addition of angular momentum to the propellant. The angular momentum is given to the propellant during spin up and is given to the product gases as the propellant burns. The angular momentum of the gases contribute no useful thrust to the motor since the angular component of momentum is directed normal to the central axis of the motor.

The theory of the flow in a rotating rocket motor is primarily concerned with the conservation of the angular momentum of the flow and determining its effects upon the mass flow and thrust producing capabilities of the nozzle. Depending upon the type of rocket motor, two types of vortices illustrated in Figure 13 can be established in the chamber. In the case of an end-burning grain the combustion gases obtain a tangential velocity component which is proportional to the radius. Therefore, a solid body vortex is established at the propellant surface. Since the motor is rotating at the same angular velocity as the gases, the solid body vortex might remain relatively intact up to the nozzle inlet. It should be noted that this type of flow is rotational since the circulation is a function of radius. Therefore, the flow is not homentropic. This type of flow has been studied with various approximations by Bastress[3], Manda[4] and King[5].

In the case of the internal burning grain all combustion gases leave the surface of the propellant with the same tangential velocity. This causes each streamline in the flow to possess the same angular momentum. Therefore, as the stream lines approach the center line they must increase their tangential velocity to conserve angular momentum. This type of flow is a free vortex in which the entire flow field is homentropic. This case was first studied by Binnie[6] in 1949, and later by Mager[7] in 1961.

In actual flow fields, it is found that the free vortex changes to a forced vortex near the centerline due to the large velocity gradients, as shown in Figure 13. In fact, a great deal of experimental study related to the Ranque-Hilsch vortex tube indicates that a free vortex will very quickly transform into a forced vortex. The rate of conversion depends

upon the viscosity of the fluid and the turbulence level of the flow, as well as boundary conditions such as the rate of mass injection into the cylinder.

With this brief introduction to the general problem of the effect of high acceleration upon the internal ballistics of solid propellant rocket motors, the analytical studies which have been made will be presented.

B. Analysis of Rotating Flow in Nozzles

The analytical efforts have been concentrated upon the fluid mechanics of rotating flows. In particular, the effect of rotation upon the mass flow and thrust producing capabilities of the nozzle have been studied most extensively.

As previously discussed, there are two possible types of vortex flows in rotating rocket motors depending upon the grain configuration. The end-burning grain has been studied most extensively. However, the analysis to be discussed can be applied to either end-burning or internal burning grains if the proper initial conditions are established.

B.1. The Model

The physical model, illustrated in Figure 14, consists of a rocket motor rotating with a constant angular velocity, ω_o. The flow field is composed of a number of stream shells of annular cross section, each of which possesses a fixed amount of energy and momentum.

The following assumptions are made as to the nature of the flow.

1. The flow is inviscid.
2. The flow is adiabatic.
3. The flow is steady.
4. The flow is axisymmetric.
5. Radial velocities are negligible.

Since the flow in an end-burning rocket is a forced vortex at the propellant surface, the stagnation properties vary from one streamline to the next. However, because the flow is adiabatic and inviscid, entropy, energy, and angular momentum are conserved along a streamline. Under the assumptions listed above, there are five equations available to describe the flow field. These are:

1. Conservation of energy

$$c_p T_o = c_p t + \frac{w^2 + v^2}{2} = \text{const. along streamlines} \qquad (1)$$

2. Conservation of angular momentum

$$V \cdot r = \Gamma = \text{const. along streamlines} \qquad (2)$$

3. Conservation of mass

$$d\dot{m} = 2\pi\rho w r dr \qquad (3)$$

4. Conservation of radial momentum

$$\frac{dp}{dr} = \rho \frac{v^2}{r} \qquad (4)$$

5. Equation of state

$$p = \rho R t \qquad (5)$$

The solution is obtained by proceeding downstream from the propellant surface starting with the given initial conditions to determine the radius of the outermost streamline and the distribution of the properties in the radial direction at each axial position. The equations involve the five unknowns p, ρ, t, w, v which are functions of the radius at each axial position.

B.2. The Simplified Analysis

As a first approximation to the problem of determining the flow properties in the nozzle, it was decided that a degree of simplification could be obtained by considering the two limiting cases.

1. Allow the axial velocity, W, to be an independent variable.
2. Allow the angular velocity, ω, to be an independent variable.

In this way, either W or ω could be specified at a plane downstream of the the nozzle inlet, thus permiting the integration of the conservation equations at that location.

A serious difficulty resulted from this simplification, since one of the governing equations had to be neglected. Because the conservation of energy, mass, and angular momentum seemed most significant to the objectives of the investigation, the radial momentum equation was disregarded. The problem then reduces to one of the following two cases. For constant axial velocity in a plane,

$$p, \rho, t, v = f(r,w) \tag{6}$$

and for constant angular velocity in a plane,

$$p, \rho, t, w = f(r,\omega) \tag{7}$$

The initial conditions for these calculations were determined quite arbitrarily by assuming that at the nozzle inlet there existed a uniform static pressure and temperature, while the stagnation properties varied with radius due to the kinetic energy variation associated with the tangential velocity variations. The tangential velocity was determined from the spin rate of the motor, and the axial velocity profile was assumed to be uniform.

B.3 Constant Axial Velocity

There is perhaps no physical justification for the treatment of this case. However, when compared to the case of constant angular velocity, it yields results which are useful in judging the applicability of the simplified approach for predicting the nozzle performance.

This problem was solved by assuming progressively larger values of the axial velocity, w. At each plane associated with this velocity the governing equations are then integrated numerically across the stream-shells whose stagnation properties were derived from the initial conditions of the flow. It was necessary to compute iteratively the angular velocity in each stream shell so that all the governing equations were satisfied. The remaining flow properties were determined as a function of radius until the conditions in every steamshell were known.

Associated with every assumed axial velocity there is a wall radius which is given by the limiting streamline. This wall radius decreases with increased axial velocity until a minimum radius is found such that

$$\frac{dR_{wall}}{dw} = 0 \tag{8}$$

In this manner, a minimum radius can be determined as a function of the initial spin rate and the other initial chamber conditions. A generalized design chart based upon this case is presented in Figure 15.

B.4. Constant Angular Velocity

This case is of considerable interest in that a constant angular velocity at a plane in the nozzle requires a solid body vortex to exist. The stress between adjacent stream shells in zero, as shown by the following equations.

$$\tau = \mu \left(\frac{\partial v}{\partial r} - \frac{v}{r}\right) \tag{9}$$

$$v = r\omega \tag{10}$$

$$\tau = \mu (\omega - \omega) = 0 \tag{11}$$

For any disturbance away from a solid body vortex, the effect of viscosity is to restore the solid body nature of the vortex provided wall shear is neglected.

The computations proceed in a manner similar to the previous case. Successively larger values of the angular velocity are assumed. At each plane defined by a fixed angular velocity, the properties of each stream shell were determined by integrating the governing equations. In this manner the properties of each streamline could be determined, as well as the radius of the outer wall. A typical set of results is presented in Figure 16.

Contrary to the constant axial velocity case, the angular velocity, ω, is not a continuously increasing function. After a minimum radius is obtained, the angular velocity should increase as the flow expands into the diverging portion. Therefore, the minimum throat area was located by computing for each value of ω, two solutions corresponding to the supersonic and the subsonic portion of the flow field. There should exist a unique critical angular velocity ω_c such that the upstream and downstream axial velocity matched. However, the arbitrary nature of the initial conditions and the neglect of the radial momentum equation prohibited the matching of the axial velocities across the entire radius at the critical position. This discontinuity in the flow properties became more pronounced with higher motor spin rates. Despite this obvious fallacy in the analysis, the results did not significantly differ from those of the constant axial velocity case.

The difficulties discussed above led to the conclusion that the simplified approach was seriously overspecified. The simplified approach is similar to those of Bastress[3] and Manda[4] which are reviewed in Reference 1. Therefore, a more complete and consistent model was postulated.

B.5. The Complete Model

This model is essentially the same as the simplified model with the radial momentum equation being retained. The addition of the radial momentum equation allows all the dependent variables to be functions of the one in dependent variable, the radial position.

$$p, \rho, t, w, v = f(r) \tag{12}$$

The governing equations are those given by Eqs. (1)-(5). It may be observed that three of these equations (energy, angular momentum, and state) are algebraic relationships along streamlines. The two remaining equations (mass and radial momentum) are ordinary differential equations of the first order when the radial velocities are neglected. It follows that the three algebraic equations can be used to reduce the entire set of equations into two total differential equations.

Since the flow is isentropic and adiabatic, the following relationship between the thermodynamic properties along a streamline is applicable.

$$P = \rho^{\gamma} \cdot C(\psi) \tag{13}$$

where $C(\psi)$ is a function of the streamline being considered.

The angular momentum and the energy are also functions of the streamlines only and their magnitude is determined from the intital conditions at the propellant burning surface.

$$\Gamma = \Gamma(\psi) = v \cdot r \tag{14}$$

$$E = E(\psi) = c_p T_o = c_p t + \frac{w^2 + v^2}{2} \tag{15}$$

The mass flow rate is given by Eq. (3).

$$d\dot{m} = 2\pi\rho w r dr \tag{16}$$

Dividing Eq. (16) by the total mass flow, $\dot{m}_o$, the following expression is obtained.

$$\frac{dm}{\dot{m}_o} = d\psi = \left(\frac{2\pi}{\dot{m}_o}\right) \rho w r dr \tag{17}$$

or

$$\dot{\psi} = \frac{d\psi}{dr} = \left(\frac{2\pi}{\dot{m}_o}\right) \rho w r \tag{18}$$

From Eq. (1),

$$w^2 = [(E(\psi) - c_p t)\, 2 - v^2] \tag{19}$$

Substituting Eq. (14) for V^2 into Eq. (19) gives

$$w^2 = \left[(E(\psi) - c_p t)\, 2 - \frac{r^2(\psi)}{r^2}\right] \tag{20}$$

From Eq. (13)

$$t = p/\rho R = \frac{p^{\frac{\gamma-1}{\gamma}}}{RC(\psi)^{1/\gamma}} \tag{21}$$

Finally, when Eq. (21) is introduced into Eq. (20) an expression for the axial velocity is obtained as a function of P, ψ, and r.

$$w = \left[(E(\psi) - \frac{c_p}{R} \frac{p^{\frac{\gamma-1}{\gamma}}}{C(\psi)^{1/\gamma}}\right]^{1/2} \tag{22}$$

By substituting Eq. (22) and Eq. (13) into Eq. (17), the following expression is obtained.

$$\dot{\psi} = \frac{d\psi}{dr} = \left(\frac{2\pi}{\dot{m}_o}\right) \cdot \frac{p^{1/\gamma}}{C(\psi)^{1/\gamma}} \cdot \left[(E(\psi) - \frac{c_p}{R} \cdot \frac{p^{\frac{\gamma-1}{\gamma}}}{C(\psi)^{1/\gamma}}\right) 2 - \frac{r^2(\psi)}{r}\Big]^{1/2} \tag{23}$$

In a similar manner the radial momentum equation can be expressed as a function of P, ψ, and r.

$$\dot{p} = \frac{dp}{dr} = \frac{p^{1/\gamma}}{C(\psi)^{1/\gamma}} \cdot \frac{r^2(\psi)}{r^3} \tag{24}$$

Therefore, there exist two simultaneous differential equations involving two dependent variables, ψ and P, as a function of the independent variable, r. These equations are given below where the following substitution is made for convenience.

$$D(\psi) = C(\psi)^{-1/\gamma} \tag{25}$$

$$\dot{\psi} = \dot{\psi}(\psi,P,r) = \left(\frac{2\pi}{m_o}\right) \cdot P^{1/\gamma} \cdot D(\psi) \left[\left(E(\psi) - \frac{c_p}{R} \cdot P^{\frac{\gamma-1}{\gamma}} \cdot D(\psi)\right) 2 - \frac{\Gamma^2(\psi)}{r^2}\right]^{1/2} \tag{26}$$

$$\dot{P} = \dot{P}(\psi,P,r) = P^{1/\gamma} \cdot D(\psi) \cdot \frac{\Gamma(\psi)^2}{r^3} \tag{27}$$

These equations may be solved numerically at any downstream plane provided a consistent set of initial conditions are supplied. The initial conditions should allow the functions D, Γ, and E to be expressed as a function of ψ alone. It should be noted that if the downstream plane to be considered is a region of zero radial velocity the equations are exact, since for adiabatic, inviscid flow the history of the flow between the initial conditions and the final conditions does not influence the final conditions. Therefore, the desired result is the value of the downstream properties in a plane of zero radial velocity. A schematic of this case is shown in Figure 17.

The method for obtaining a nozzle solution is to determine a downstream plane for the given initial conditions for ψ and P at the burning surface. The radius at which $\psi = 1.0$ is then computed for different axial locations until a minimum wall radius is obtained. This wall radius would then be the "throat" radius of the nozzle in a flow derived from the initial conditions determined at the propellant surface. The approximation of zero

radial velocities should not be significant, especially when the throat radius of curvature of the nozzle is large.

B.6. Initial Conditions for an Rotating End Burning Rocket Motor

Consider an end-burning rocket motor rotating at an angular velocity ω_o. This motor is operating at steady state conditions with a centerline pressure at the propellant surface of P_1.

The stagnation temperature of the gases leaving the propellant surface is given by,

$$T_o = t + \left(\frac{v^2 + w^2}{2}\right) \cdot \left(\frac{\gamma - 1}{\gamma R}\right) \tag{28}$$

The energy of the combustion gases is given by

$$T_o = T_f + \frac{v^2}{2} \left(\frac{\gamma - 1}{\gamma R}\right) \tag{29}$$

where T_f is the flame temperature of the propellant.

Combining Eqs. (28) and (29), the following equation is obtained.

$$T_f = t + \frac{w^2}{2} \cdot \left(\frac{\gamma - 1}{\gamma R}\right) \tag{30}$$

The mass flux from the propellant surface is given by

$$\rho w = a\, p^n \tag{31}$$

where,

$$a = a_o \cdot \rho_p = \text{constant} \tag{32}$$

$$[illegible] \quad (33)$$

The axial velocity at the surface is then given by

$$w = Rt\ aP^{n-1} \quad (34)$$

The above equation may be substituted into Eq. (30) to give

$$T_f = t + \frac{(Ra)^2}{2} \cdot t^2 \cdot P^{2n-2} \quad (35)$$

which, when solved for the pressure gives

$$P = \left[2 \frac{(T_f - t)}{(Ra)^2\ t^2} \right]^{\frac{1}{2n-2}} \quad (36)$$

The above equation relates the static pressure on the burning surface to the static temperature at the propellant surface.

In order to solve explicitly for temperature or pressure as a function of radius, it is necessary to consider the radial momentum equation.

$$\frac{dp}{\rho} = \frac{V^2 dr}{r} \quad (37)$$

Equation (37) can be integrated employing previously derived results. Since at the propellant surface the gases are in solid body rotation, Eq. (37) can be rewritten as follows.

$$\frac{dp}{\rho} = Rt \frac{dp}{p} = \omega_o^2\ rdr \quad (38)$$

It will be recalled from Eq. (36) that the static temperature is a function of static pressure. Therefore,

$$\int_o^r t \frac{dp}{p} = \frac{\omega_o r^2}{2R} \Big|_{\text{Rotating propellant face.}} \tag{39}$$

where,

$$p = \left[\frac{2 (T_f - t)}{(Ra)^2 \cdot t^2} \right]^{\frac{1}{2n-2}} \tag{40}$$

$$dp = \left(\frac{1}{2n-2}\right) \cdot \left(\frac{2}{(Ra)^2}\right) \cdot \left(- 2 T_f t^{-3} + t^{-2}\right)^{\left(\frac{1}{2n-2} - 1\right)} \tag{41}$$

Therefore,

$$\int_o^r t \frac{dp}{p} = \frac{\omega_o^2 r^2}{2R} = \frac{T_f}{2(1-n)} \left[- \ln \left(\frac{1-T^*}{1-T_1^*}\right) + (T^* - T_1^*) \right] \tag{42}$$

where, $T^* = t/T_f$

Finally,

$$T^* = \left[\ln \left(\frac{1-T^*}{1-T_1^*}\right) + \frac{\omega_o^2 r^2 (1-n)}{T_f R} + T_1^* \right] \tag{43}$$

The above relationship is a transcendental equation relating temperature to radius which can be solved numerically. It can be shown that the variation of T^* is not great, and that T^* must be between.

$$T_1^* < T^* < 1.0 \tag{44}$$

It is now a simple matter to determine the variation of the remaining thermodynamic properties by integration. The results are given below.

$$\int \frac{dp}{p} = \int \frac{\omega_o^2 r dr}{2R\, T(r)} \tag{45}$$

$$P(1,j) = P_1 \, e^{\int_0^r \frac{\omega_0 r dr}{2 \cdot R \cdot T(r)}} \tag{46}$$

$$W(1,j) = a \cdot R \cdot T(1,j) \cdot P_{(1,j)}^{n-1} \tag{47}$$

$$V(1,j) = \omega_0 \cdot r(1,j) \tag{48}$$

$$To(1,j) = t(1,j) + \frac{W^2(1,j) + V^2(1,j)}{2 \, c_p} \tag{49}$$

$$Po(1,j) = P(1,j) \cdot \left(\frac{To(1,j)}{t(1,j)}\right)^{\frac{\gamma-1}{\gamma}} \tag{50}$$

$$\dot{m} = 2\pi \int_0^r \rho(1,j) \, W(1,j) \cdot r \cdot dr \tag{51}$$

In addition to the initial properties on the propellant surface, the functions

$$D(\psi) = (P^{1/\gamma}/\rho) \tag{52}$$

$$E(\psi) = c_p \, To(1,j) \tag{53}$$

$$\Gamma(\psi) = \omega_0 \cdot r^2(1,j) \tag{54}$$

can be determined and fitted to an appropriate polynomial in ψ. Once these polynomials are obtained, the integration of the governing equations at a downstream plane can be completed.

$$D(\psi) = d_1 + d_2\psi + d_3\psi^2 + d_4\psi^3 + \cdots \tag{55}$$

$$E(\psi) = e_1 + e_2\psi + e_3\psi^2 + e_4\psi^3 + \cdots \tag{56}$$

$$\Gamma(\psi) = \gamma_1 + \gamma_2\psi + \gamma_3\psi^2 + \gamma_4\psi^3 + \cdots \tag{57}$$

C. Proposed Future Work

The analysis developed in section II.B.5 will be programmed for numerical solution. Initial conditions as derived in section II.B. 6 for the end-burning rocket motor will be employed for the first of these calculations. The program will allow the calculation of the minimum throat area and the nozzle flow field for a number of propellant formulations, chamber conditions, and motor spin rate. It is expected that these results can then be correlated into generalized charts suitable for design purposes.

Concurrent to the calculation of the properties of spinning-end burning rocket motors, the initial conditions for the internal-burning motor will be developed. As discussed in section II.B, the internal-burning motor is more subject to viscous effects, especially near the centerline. It is expected therefore, that viscous effects must be taken into account.

There are several analyses available for the case of a rotating, porous cylinder in which fluid is injected through the walls. (References 8, 9, 10, 11, 12). These studies, which are discussed in Reference 1 are primarily for incompressible, laminar flow. Since the Mach number in the chamber should not be large, it is felt that an analysis of this type may be modified for an internal-burning motor. Therefore, a set of initial conditions for the nozzle inlet can be obtained and employed in the computer program developed for the end-burning motor.

Finally, it is anticipated that the effects of viscosity can be studied qualitatively by developing an approximate viscous analysis. The results of this study would then be compared to the inviscid analysis developed in section II.B.2. In this way, the effects of viscosity upon the flow in a spinning rocket motor can be studied.

IV. NOMENCLATURE

English Symbols

$a = \rho_p \dot{r}/p^n = a_o \rho_p$

$a_o = a/\rho_p$

c_p = specific heat at constant pressure

D = function of the streamline defined in eq. (52)

E = energy, a function of the streamline

$\dot{m}$ = mass flow rate

n = burning rate index

p = static pressure

R = perfect gas constant

r = radial space coordinate

$\dot{r}$ = propellant burning rate

t = static temperature

T_f = flame temperature

u = radial velocity

v = tangential velocity

w = axial velocity

Greek Symbols

Γ = angular momentum of a streamline

γ = ratio of specific heats

π = 3.14159 ...

ρ = density

ω = angular velocity

Subscripts

1 = initial condition at the propellant surface

c = critical value

o = stagnation condition

* = reduced value

p = propellant

f = flame

V. REFERENCES

1. Norton, D. J., Farquhar, B. W., Hoffman, J. D., "Analytical Studies of the Interior Ballistics of Spin Stabilized Rocket Motors - A Literature Survey," Jet Propulsion Center, Purdue University, Report No. TM-67-1 (January 1967).

2. Farquhar, B. W., Norton, D. J., Hoffman, J. D., "Experimental Studies of the Interior Ballistics of Spin Stabilized Rocket Motors - A Literature Survey," Jet Propulsion Center, Purdue University, Report No. TM-67-2 (January 1967), (confidential)

3. Bastress, "Interior Ballistics of Spinning Solid-Propellant Rockets," AIAA J. Spacecraft, Vol. 2, No. 3, 455-457, (May-June 1965).

4. Manda, L., "Spin Effects on Rocket Nozzle Performance," AIAA J. Spacecraft, Vol. 3, No. 11, 1695-1696, (Nov. 1966).

5. King, M. K., "Spin Effects on Rocket Nozzle Performance," AIAA J. Spacecraft, Vol. 3, No. 12, 1812-1813, (Dec. 1966).

6. Binnie, A. M., "The Passage of a Perfect Fluid through a Critical Cross-Section or 'Throat'," Proc. Royal Society, Vol. A 197, 545-555, (1949).

7. Mager, A., "Approximate Solution of Isentropic Swirling Flow Through a Nozzle," ARS Journal, Vol. 31, No. 8, 1140-1148, (Aug. 1961).

8. Burgers, J. M., "Application of a Model System to Illustrate Some Points of the Statistical Theory of Turbulence," Proc. Acad. Sci. Amsterdam, 43, 2, (1940).

9. Rott, N., "On the Viscous Core of a Line Vortex," ZAMP 96, 543-5, (1950).

10. Donaldson, C. duPont, "Examination of the Solutions of the Navier-Stokes Equations for a Class of Three-dimensional Vortices," Part I, II, III, Aero. Res. Assoc. Princeton REport (AFOSR TN 60-1227).

11. Lewellen, "A Solution for Three Dimensional Vortex Flows with Strong Circulation," J. Fluid Mech., Vol. 14, 420 (1962).

12. Sullivan, R. D., "A Two-cell Solution of the Navier-Stokes Equations," J. of the Aerospace Sci., 767-768, (Nov. 1959).

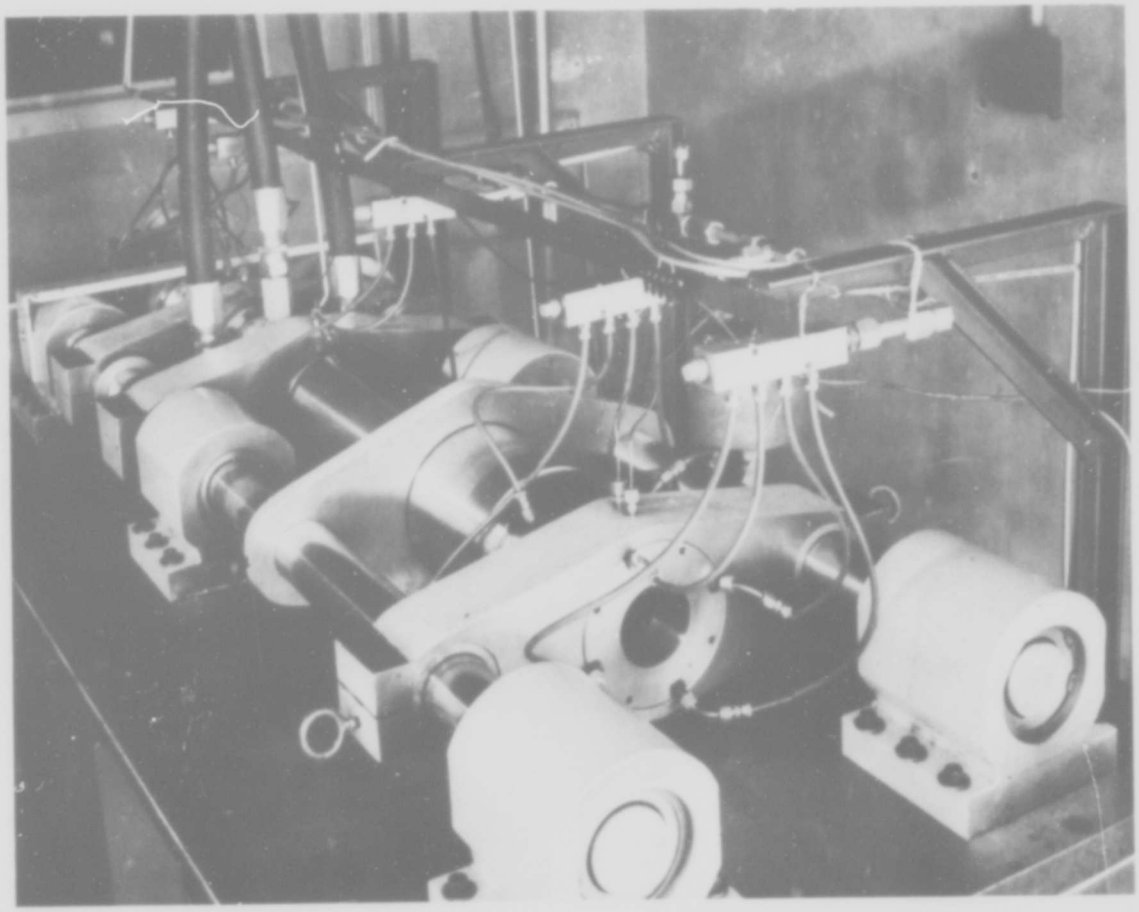

GENERAL ARRANGEMENT OF SPIN APPARATUS

FIG. 1

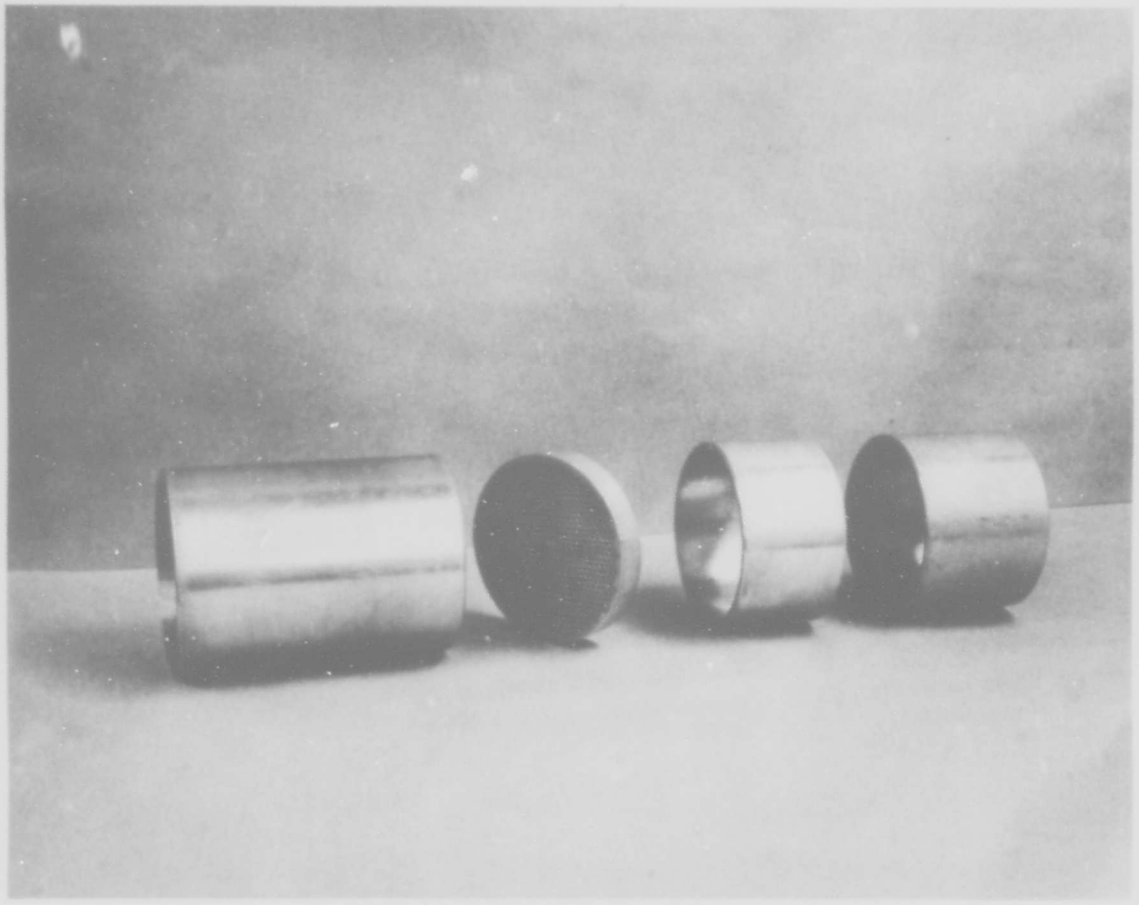

SIMULATED END BURNING GRAIN

FIG. 2

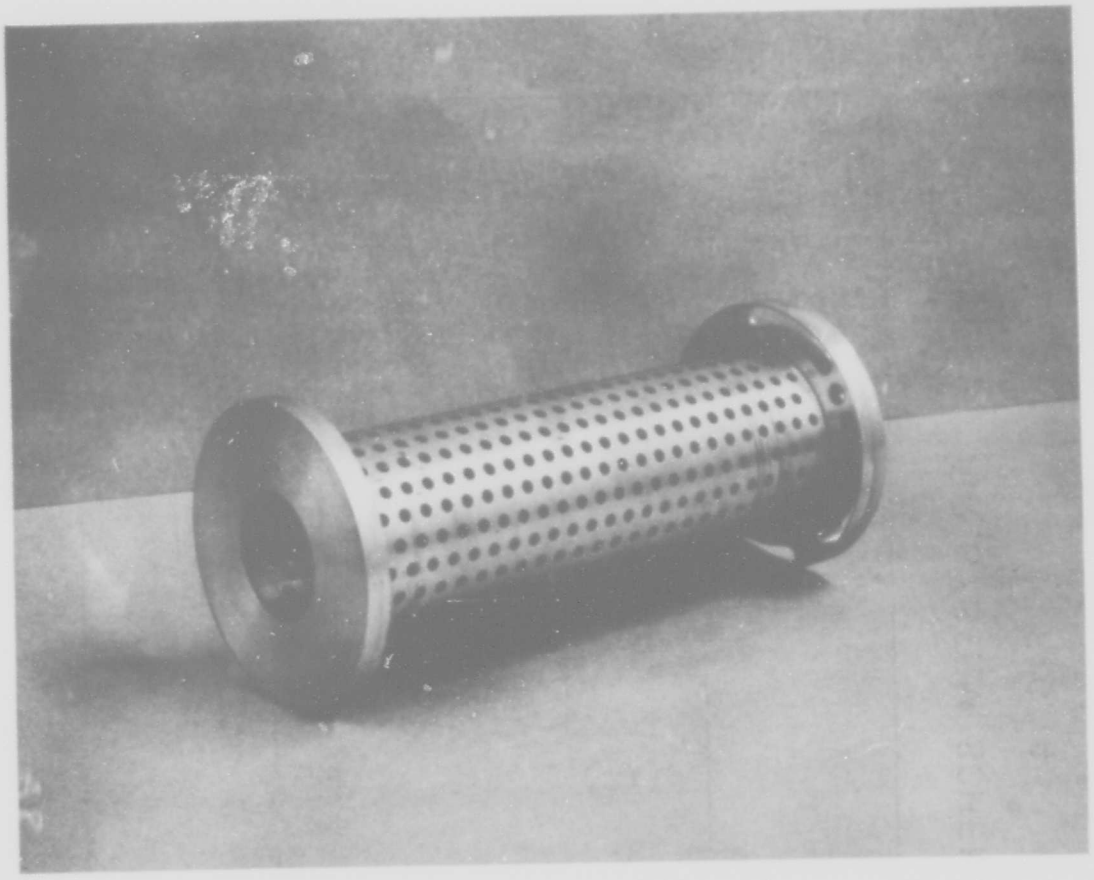

SIMULATED INTERNAL BURNING CYLINDRICAL GRAIN

FIG. 3

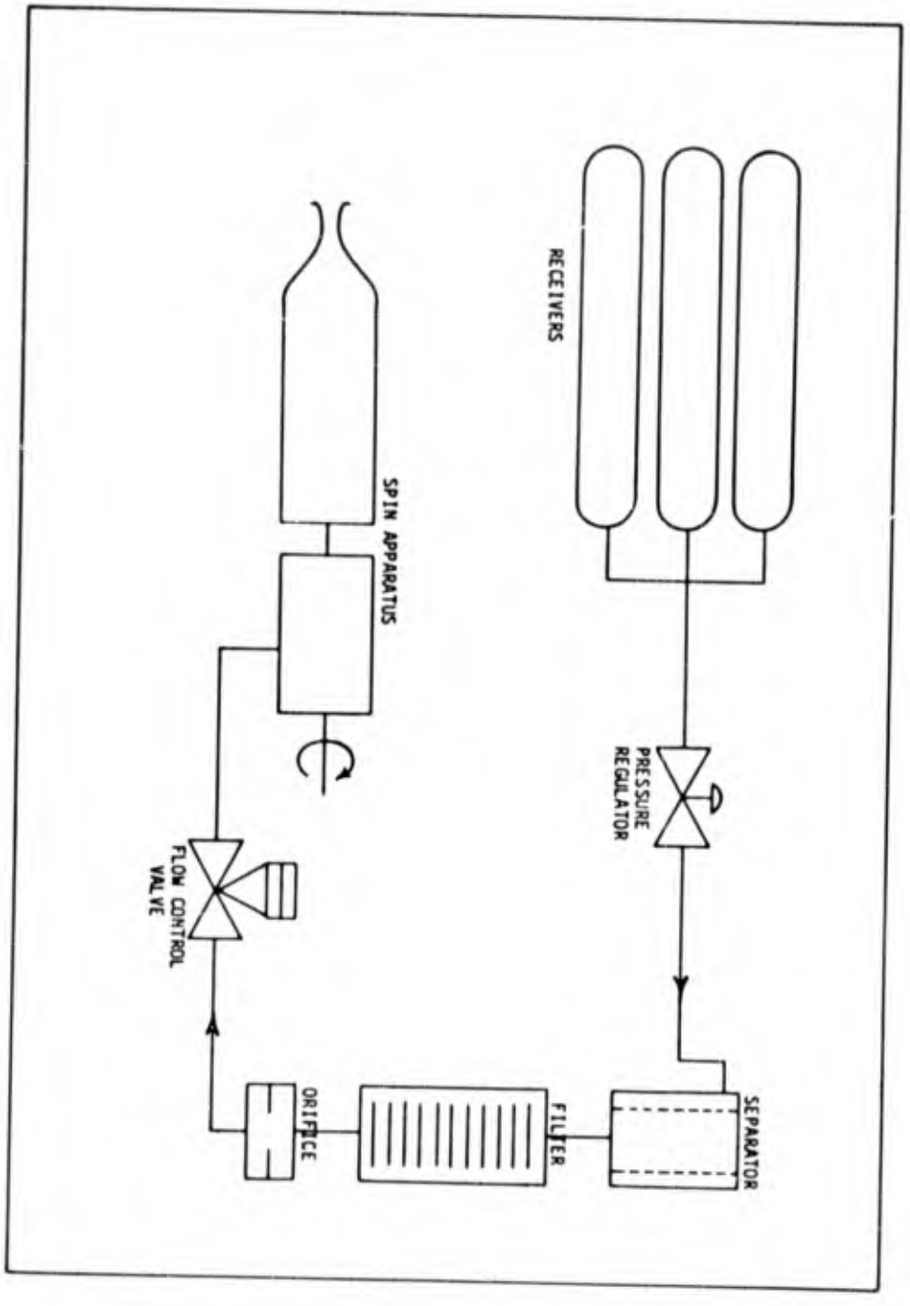

AIR SYSTEM SCHEMATIC

FIG. 4

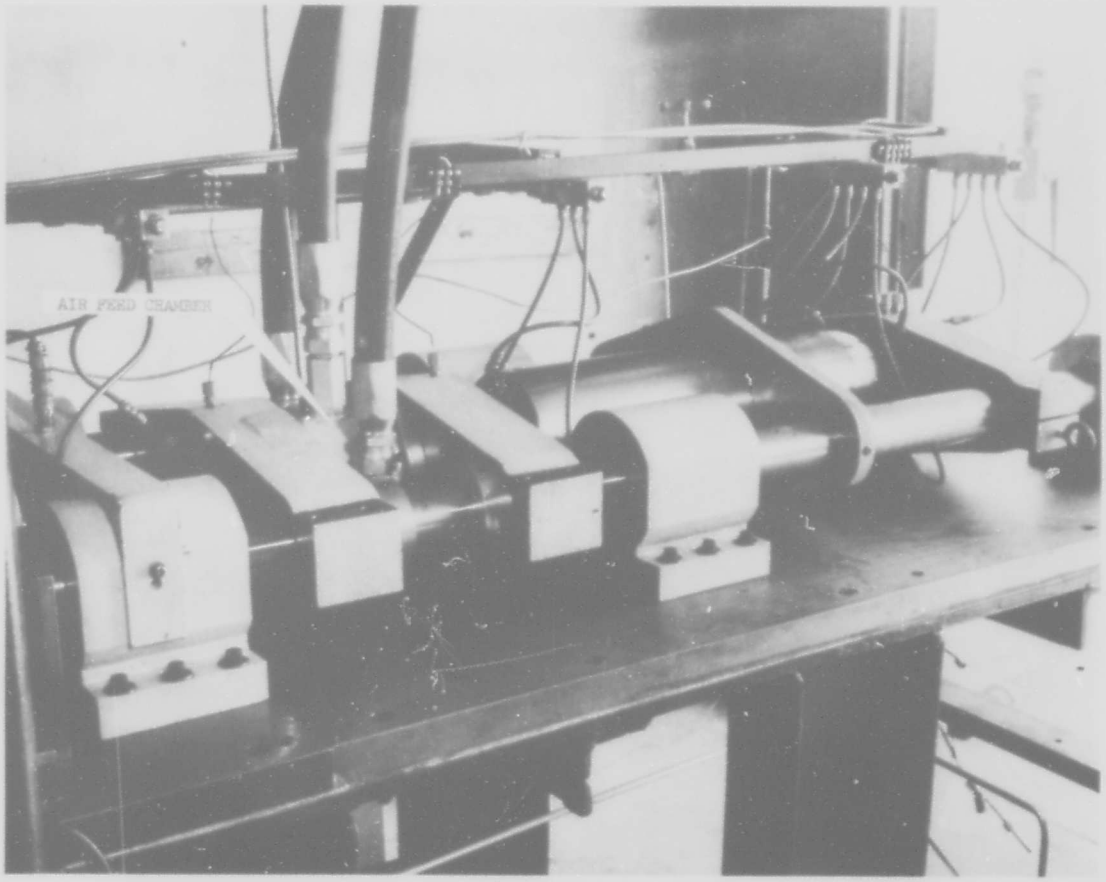

GENERAL ARRANGEMENT OF SPIN APPARATUS

FIG. 5

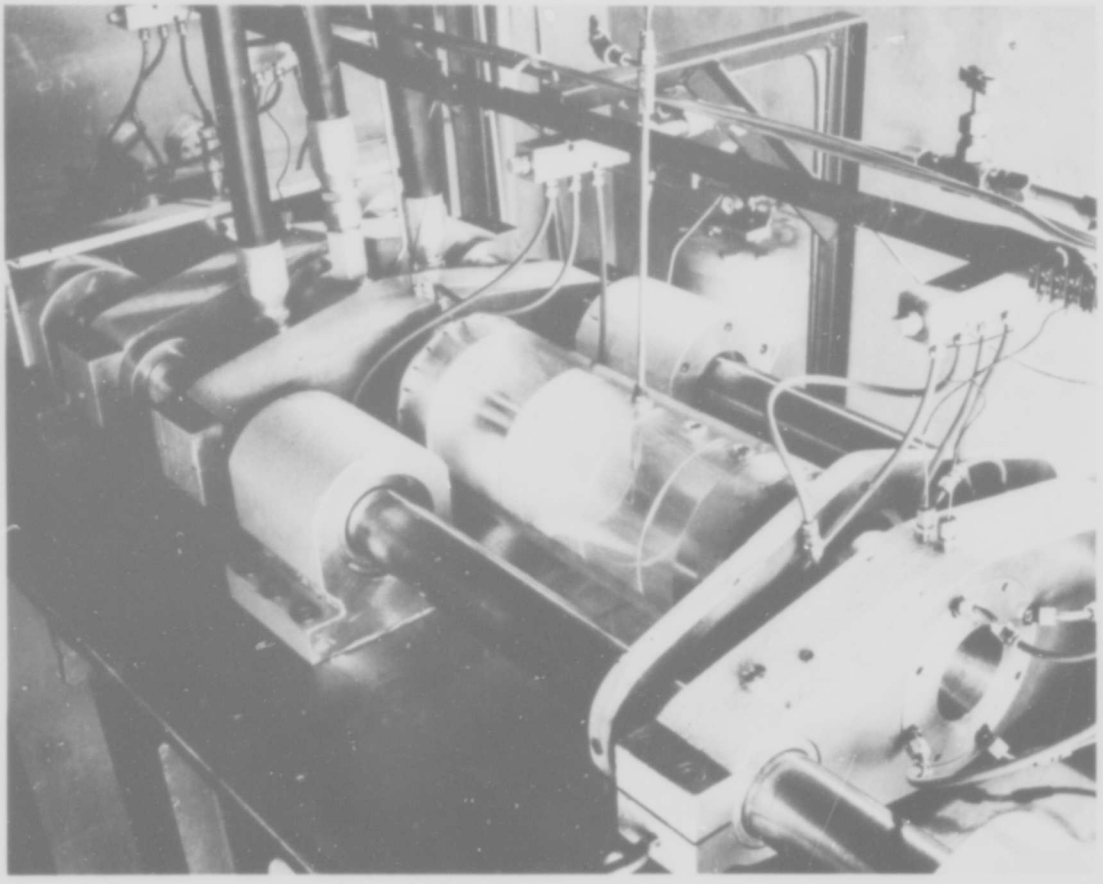

SPIN APPARATUS WITH PLEXIGLAS TEST MOTOR

FIG. 6

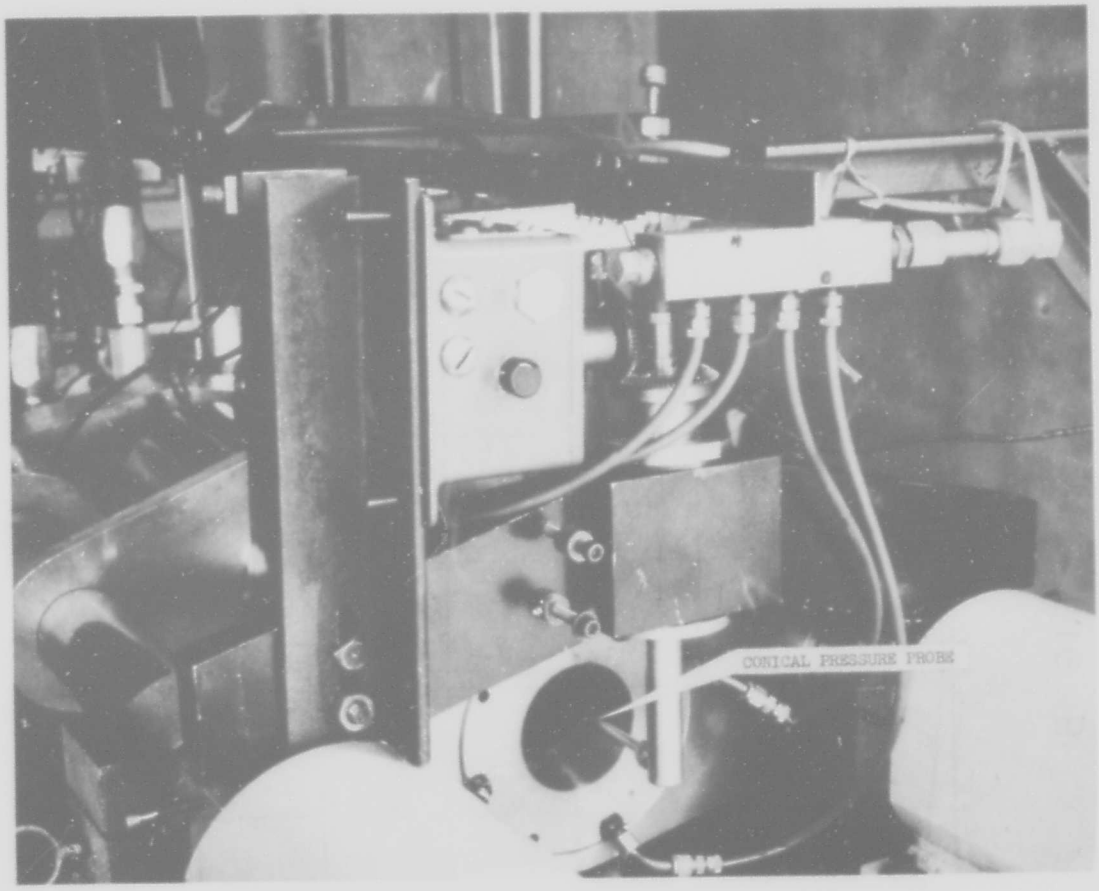

PROBE AND TRAVERSING MECHANISM

FIG. 7

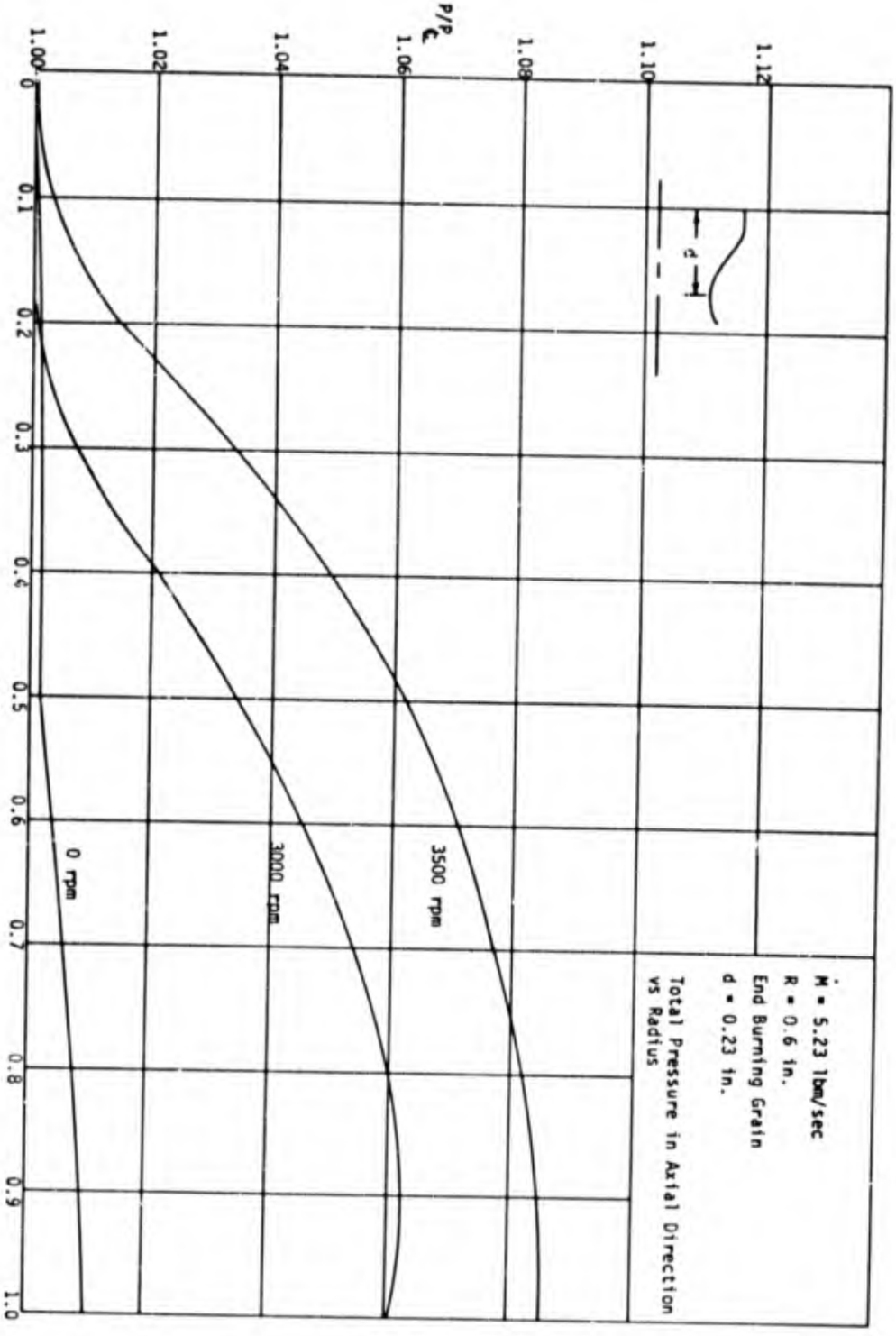
$\dot{M}$ = 5.23 lbm/sec
R = 0.6 in.
End Burning Grain
d = 0.23 in.
Total Pressure in Axial Direction vs Radius
d
3500 rpm
3000 rpm
0 rpm
P/P_c
r/R
1.00
1.02
1.04
1.06
1.08
1.10
1.12
0
0.1
0.2
0.3
0.4
0.5
0.6
0.7
0.8
0.9
1.0

FIG. 8

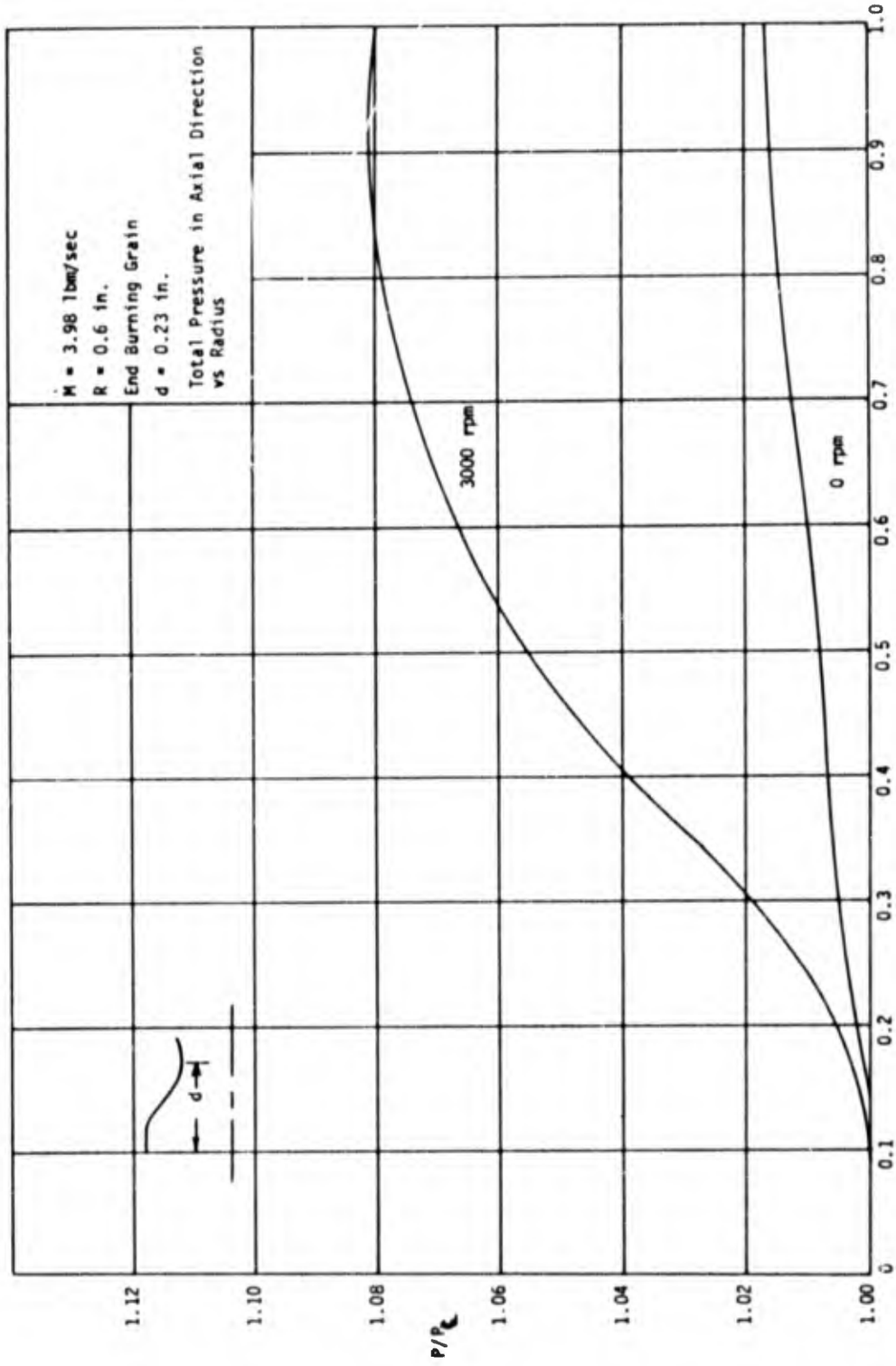
ṁ = 3.98 lbm/sec
R = 0.6 in.
End Burning Grain
d = 0.23 in.
Total Pressure in Axial Direction
vs Radius
d
3000 rpm
0 rpm
P/P_c
r/R
1.12
1.10
1.08
1.06
1.04
1.02
1.00
0
0.1
0.2
0.3
0.4
0.5
0.6
0.7
0.8
0.9
1.0

FIG. 9

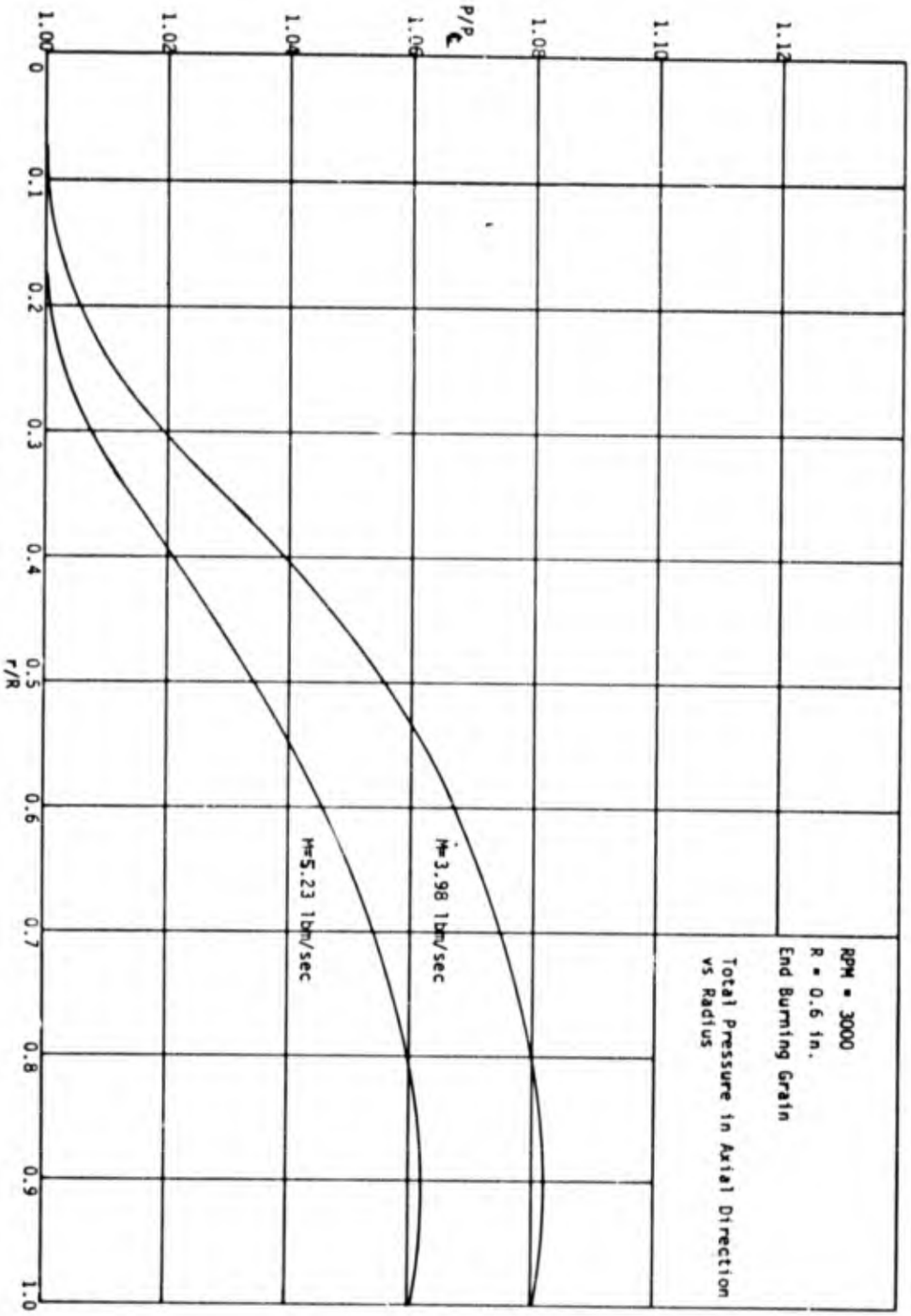
RPM = 3000
R = 0.6 in.
End Burning Grain
Total Pressure in Axial Direction vs Radius
ṁ=3.98 lbm/sec
ṁ=5.23 lbm/sec
P/Pc
r/R
1.00
1.02
1.04
1.06
1.08
1.10
1.12
0
0.1
0.2
0.3
0.4
0.5
0.6
0.7
0.8
0.9
1.0

FIG. 10

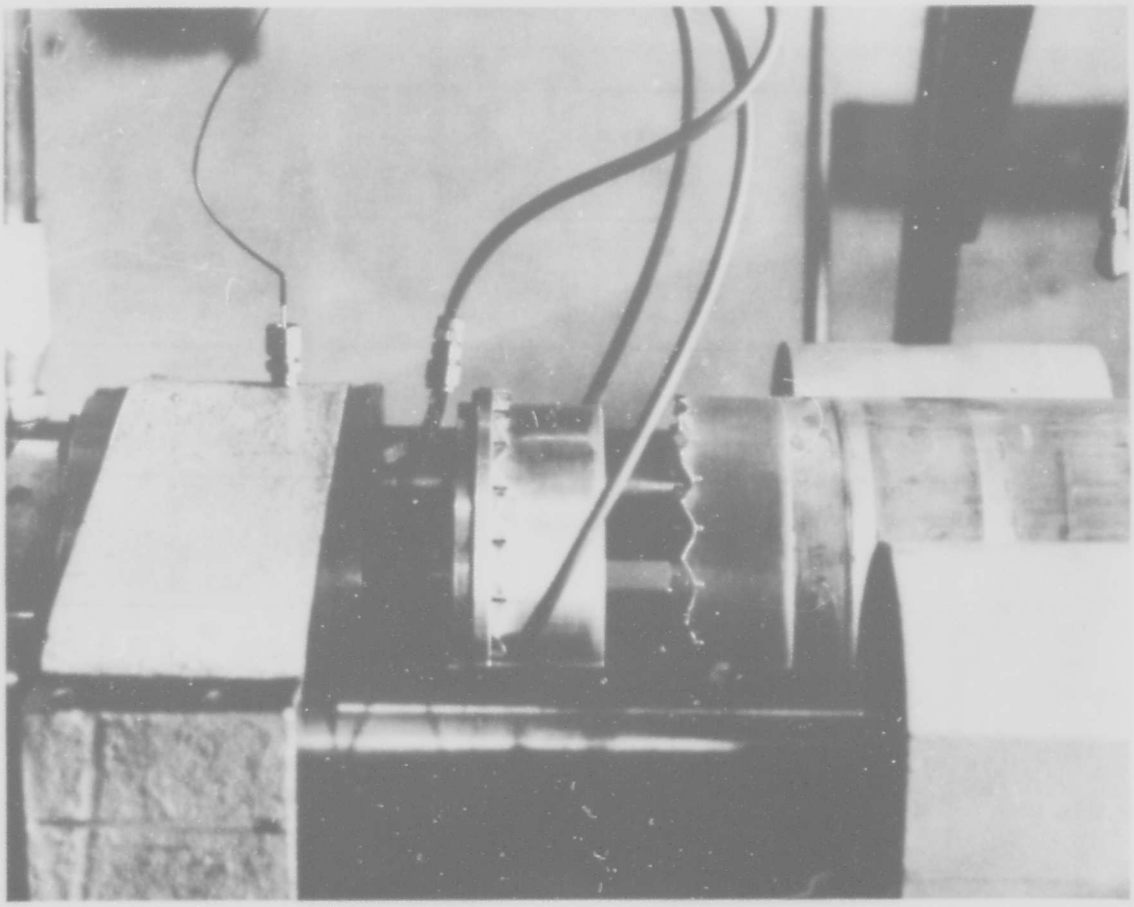

PLEXIGLAS MOTOR FAILURE

FIG. 11

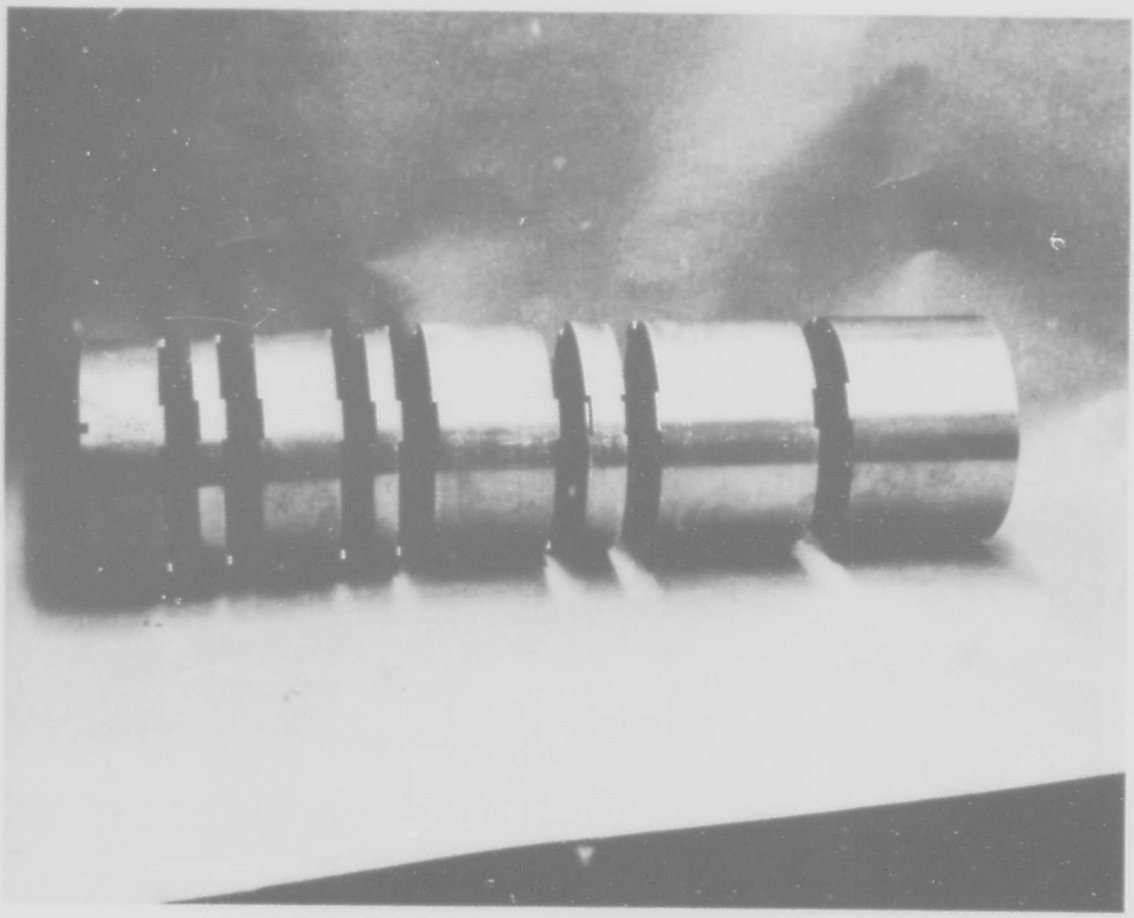

SIMULATED GRAIN INSERTS AS MODIFIED TO ELIMINATE SLIP INSIDE THE MOTOR

FIG. 12

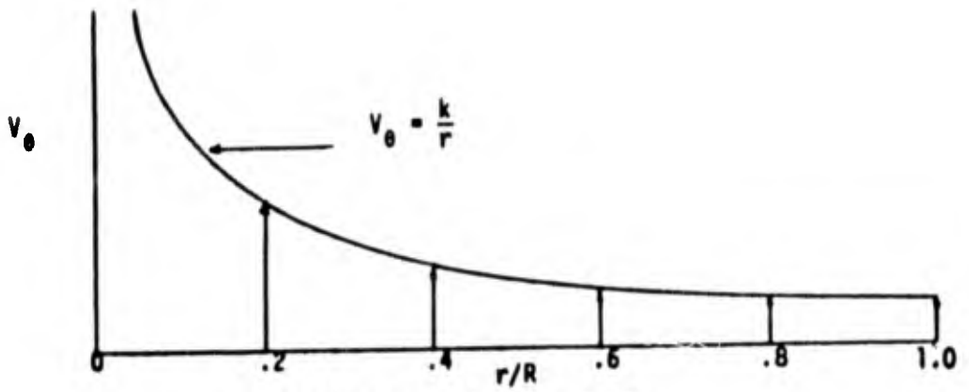

THE FREE OR POTENTIAL VORTEX

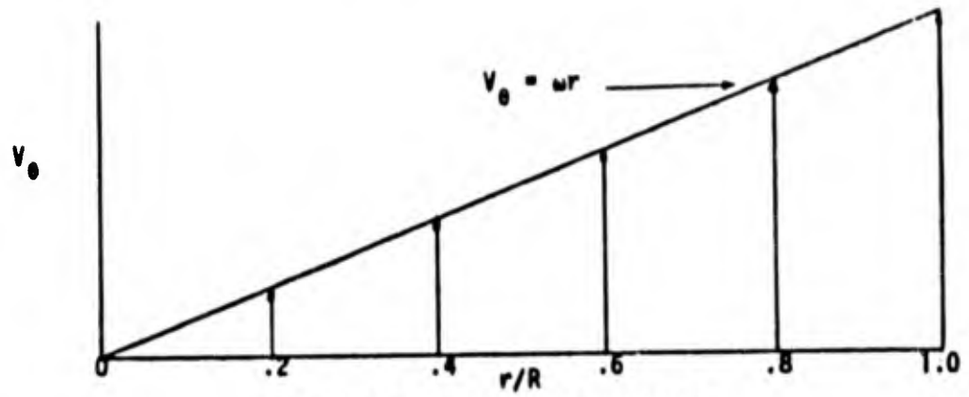

THE FORCED OR SOLID BODY VORTEX

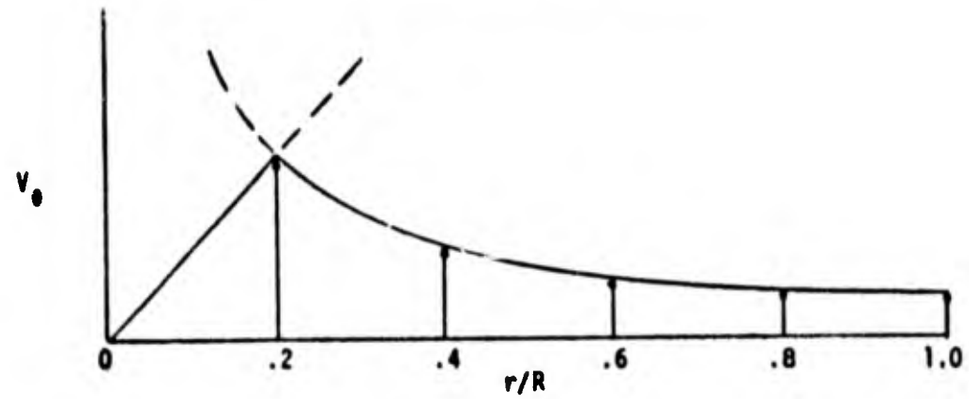

THE COMBINATION FORCED AND FREE VORTEX

FIG. 13 TYPICAL TANGENTIAL VELOCITY DISTRIBUTIONS IN VORTEX FLOWS

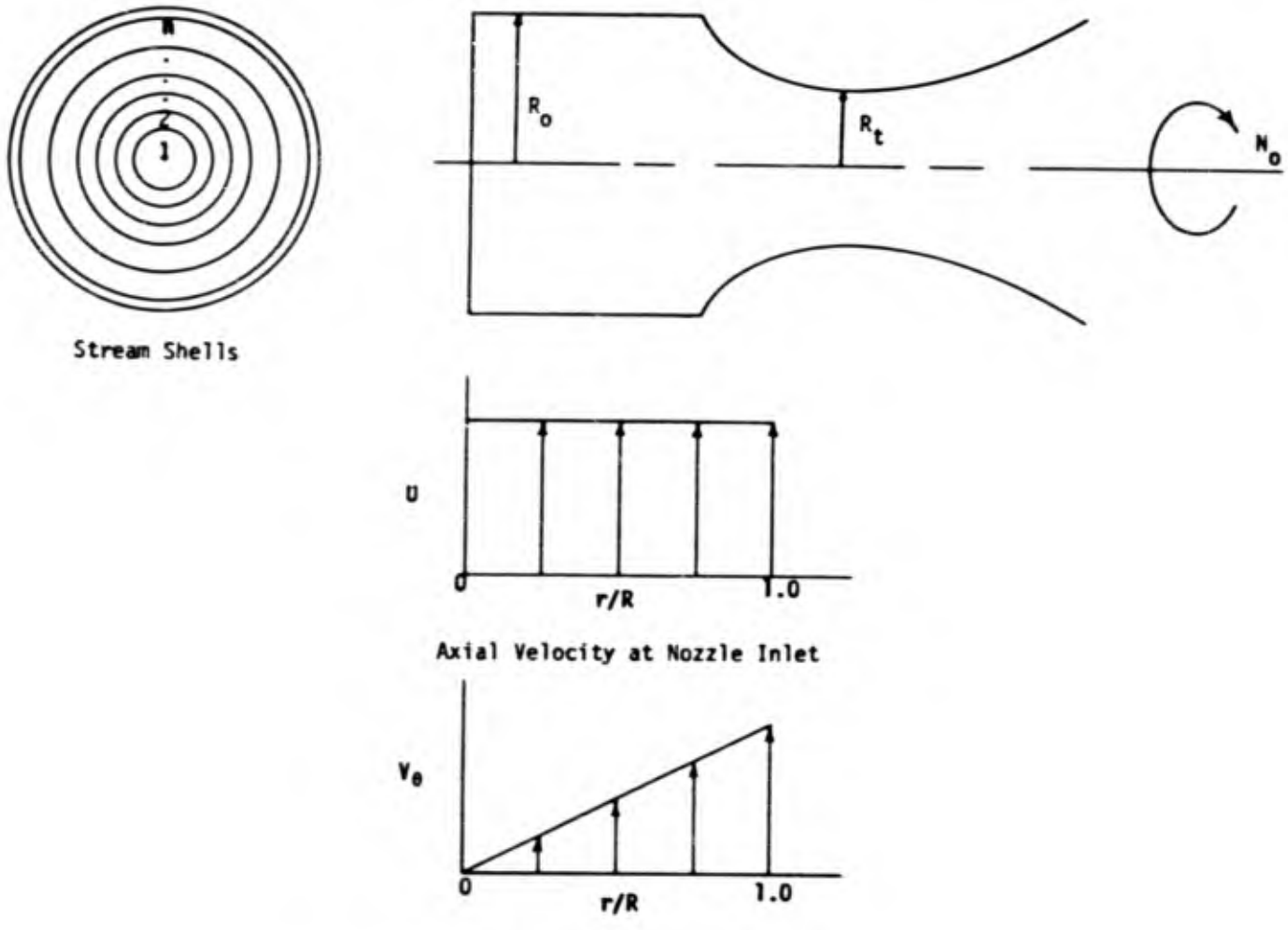

FIG. 14 THE PHYSICAL MODEL

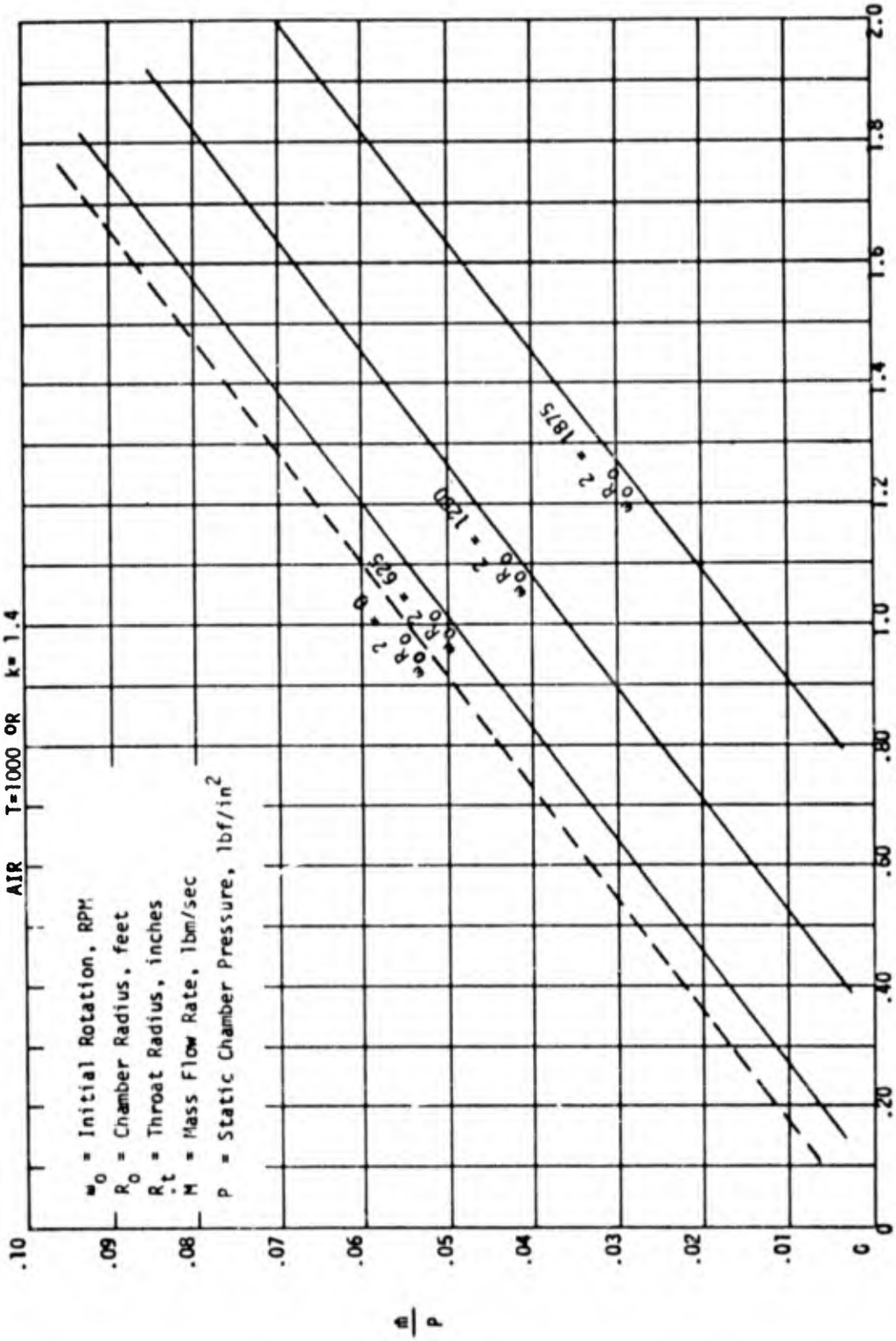

FIG. 15 $\dot{m}/P$ AS A FUNCTION OF THROAT RADIUS SQUARED FOR VARIOUS VALUES OF $\omega_o R_o^2$

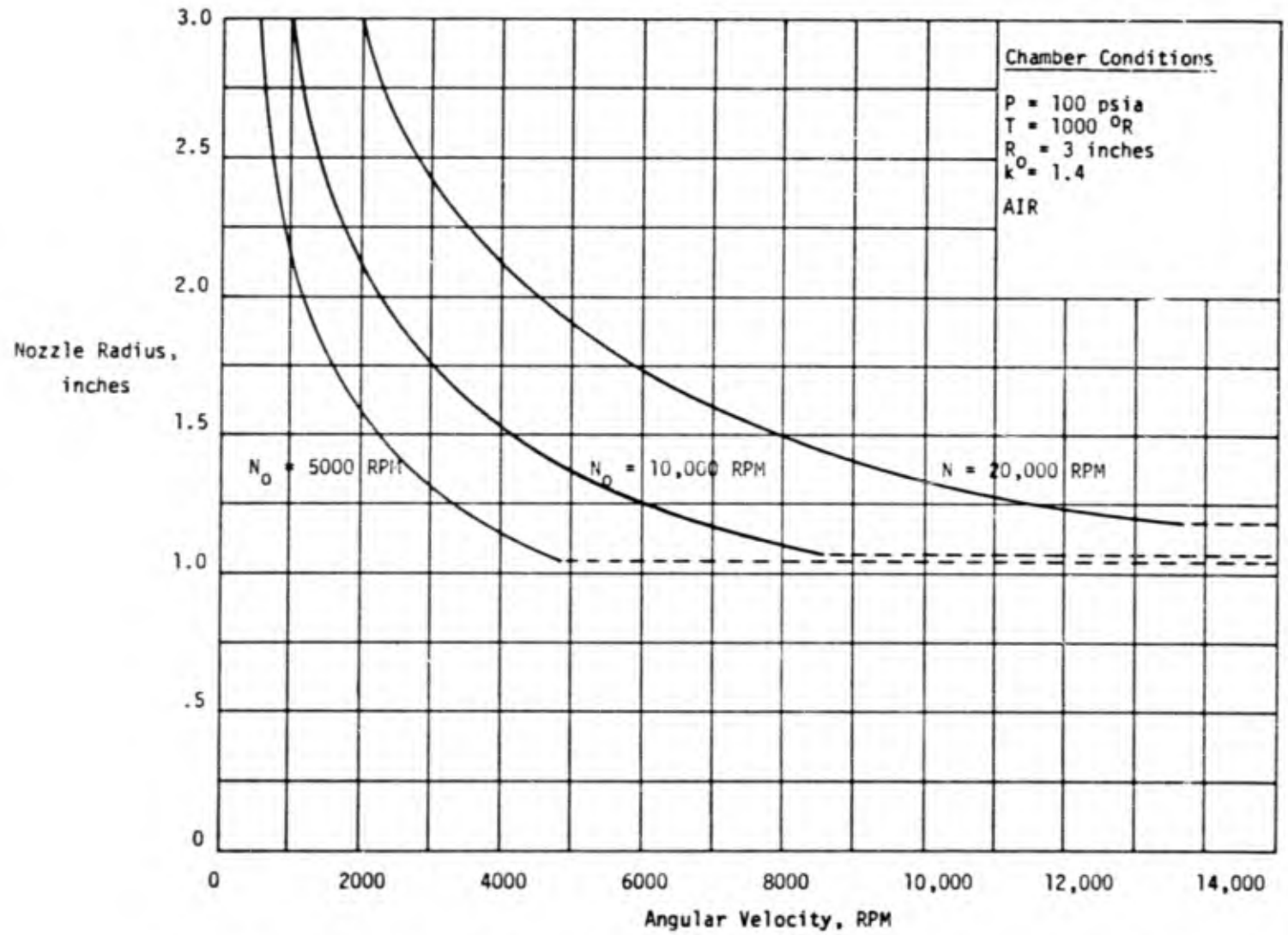

FIG. 16 NOZZLE RADIUS AS A FUNCTION OF FLOW ANGULAR VELOCITY FOR VARIOUS INITIAL SPEEDS OF ROTATION

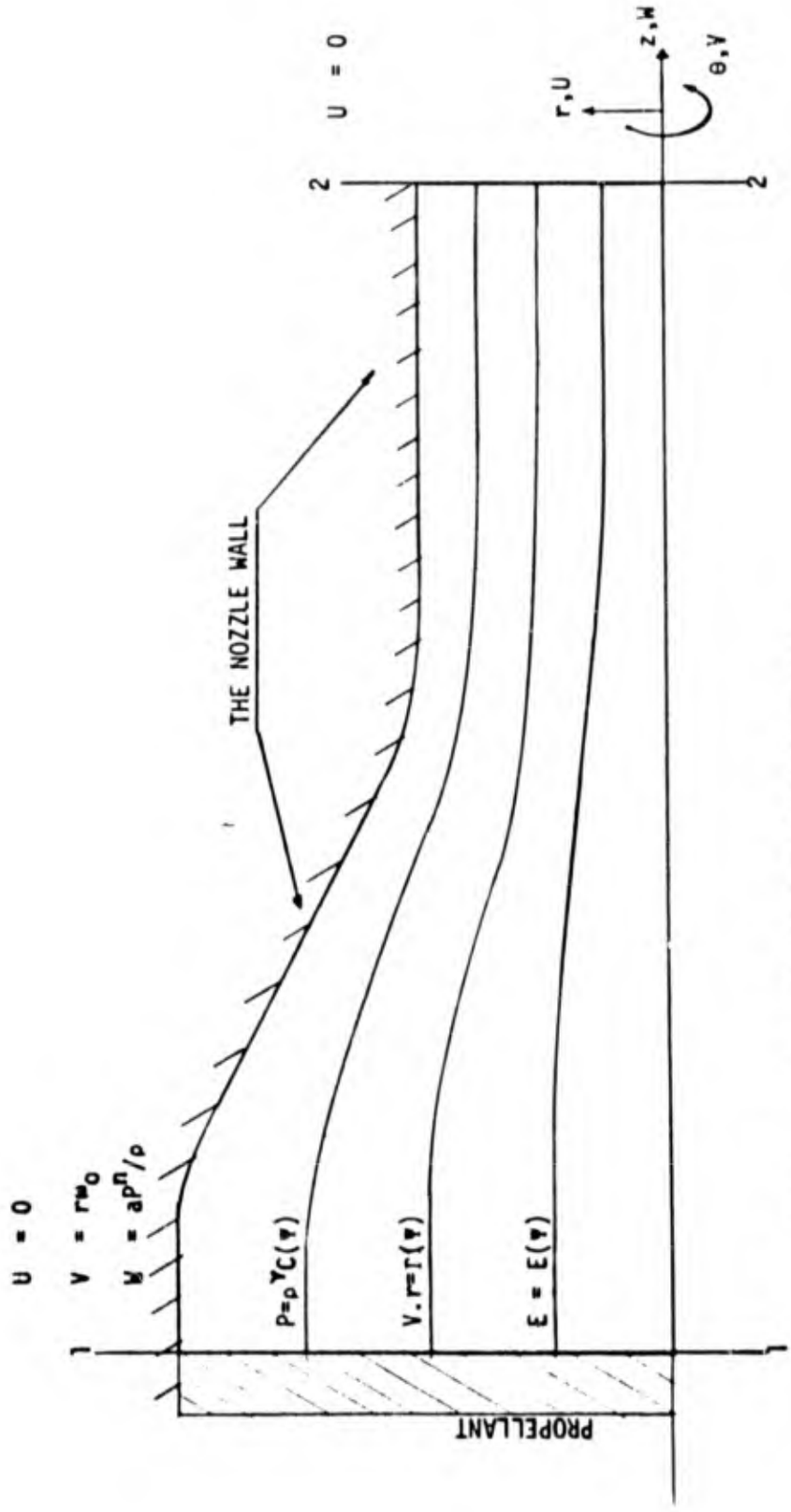

FIG 17 A SCHEMATIC OF THE COMPLETE MODEL